Dendritic synaptic integration modes under *in vivo*-like states

Cesar C. Ceballos[1], Rodrigo F. O. Pena[1,2 *]

[1] Department of Biological Sciences, Florida Atlantic University, Jupiter, FL 33458, USA

[2] Stiles-Nicholson Brain Institute, Florida Atlantic University, Jupiter, FL 33458, USA

* Corresponding author

E- mail: penar@fau.edu

Abstract

The neural code remains undiscovered and understanding synaptic input integration under *in vivo*-like conditions is just the initial step toward unraveling it. Synaptic signals generate fast dendritic spikes through two main modes of temporal summation: coincidence detection and integration. In coincidence detection, dendrites fire only when multiple incoming signals arrive in rapid succession, whereas integration involves summation of postsynaptic potentials over longer periods with minimal membrane leakage. This process is influenced by ionic properties, especially as the membrane potential approaches the firing threshold, where inactivating currents play a critical role. However, the modulation of temporal summation by these currents under *in vivo*-like conditions has not been thoroughly studied. In our research, we used computer simulations to investigate how three inactivating currents — A-type potassium, T-type calcium, and transient sodium — affect temporal summation. We found that calcium and sodium currents promote integrative behavior in dendrites, while potassium currents enhance their ability to act as coincidence detectors. By adjusting the levels of these currents in dendrites, neurons can flexibly switch between integration and coincidence detection modes, providing them with a versatile mechanism for complex tasks like multiplexing. This flexibility could be key to understanding how neural circuits process information in real time.

Introduction

It is well known that dendrites can fire sodium, calcium and NMDA dependent action potentials (dendritic spikes) under *in vivo* conditions at higher frequency than found at the soma (Moore et al 2017). These suggests the existence of dendritic synaptic integration and transformation into dendritic spikes as a first stage of neuronal processing (Ujfalussy et al 2018). Understanding the neural code involves learning how dendrites process synaptic inputs and transform them into dendritic spikes via temporal summation (Stuart et al 2015, Dembrow et al 2022). Two key summation types, coincidence detection and integration, are critical for neural coding (Brette 2015, Ratté et al 2013, Hong et al 2012, Stoll et al 2023). Coincidence detection occurs when a dendrite fires a spike after receiving multiple signals within a short interval, while integration mode allows voltage accumulation over time until a spike fires (Dembrow et al 2015, Dembrow et al 2022, Roome et al 2020). Dendrites exhibit both modes, with Purkinje neurons dendrites functioning as coincidence detectors and L5 dendrites in medial prefrontal cortex acting as integrators (Dembrow et al 2015, Roome et al 2020). These modes influence the transmission of information via firing rates or synchronized spikes (Hong et al. 2012).

These synaptic summation modes form a continuum from coincidence detection to perfect integration (Rudolph et al. 2003, Prince et al. 2021). The specific mode of summation depends on the composition of ionic currents in the dendritic membrane, which modulate synaptic temporal properties (Azouz et al. 2000, Prince et al. 2021). Strong potassium currents are linked to coincidence detection, while sodium and calcium currents support perfect integration (Mathews et al. 2010, Farries et al. 2010, Branco et al. 2016, Prescott and De Koninck 2005). Adjusting the expression of these currents allows a range of temporal summation modes.

Dendritic inactivating currents are crucial for near-threshold synaptic summation, as shown by studies on A-type potassium currents influencing theta oscillations and temporal summation (Bourdeau et al. 2007; Rathour et al. 2016). EPSPs are amplified by T-type calcium currents, enhancing temporal precision (Fukaya et al. 2018), while transient sodium currents act at subthreshold potentials (Carter et al. 2012; Stuart et al. 2015). Further research is needed to explore inactivation's role in dendritic properties.

A complete understanding requires examining currents with (i) established, (ii) less established, and (iii) inconsistent effects. (i) Non-inactivating currents like M-type potassium reduce EPSP amplitude and shorten decay (Hönigsperger et al. 2015; Peng et al. 2017; Liu et al. 2008), while persistent sodium currents amplify and prolong EPSPs (Ceballos et al. 2017b; Liu et al. 2008; Hsu et al. 2018). (ii) Inactivating currents, such as A-type potassium, consistently reduce EPSP amplitude (Hoffman et al. 1997; Mathews et al. 2010; Bourdeau et al. 2007; Rathour et al. 2016). (iii) Calcium currents show mixed effects: some studies report no impact on amplitude or decay (Stuart et al. 1995; González-Burgos et al. 2001; Andreasen et al. 1999; Hsu et al. 2018; Seong et al. 2014), others show effects on amplitude (Fukaya et al. 2018; Gillessen et al. 1997), only on decay (Prescott et al. 2005), or both (Liu et al. 2008; Connelly et al. 2016; Urban et al. 1998; Evans et al. 2017; Deleuze et al. 2012). Transient sodium currents also show variable effects: some studies report no effect (Connelly et al. 2016; Grunditz et al. 2008), while others show amplification of EPSPs (Carter et al. 2012; Hage et al. 2016) or TTX-sensitive prolonged decay (Ceballos et al. 2018). Sodium-dependent EPSP amplification has been observed *in vivo* (Hsu et al. 2018).

Most EPSP studies are not easily transferable to *in vivo* situations, where neural coding is better understood. *In vivo*, large depolarization states occur during neuronal oscillations like theta oscillations (Adam et al. 2019; Malezieux et al. 2020). These states bring the membrane potential near the threshold, suggesting the activation of inactivating currents (Hsu et al. 2018), though little is known about how these conductances affect synaptic summation *in vivo*. This raises questions about how these currents filter synaptic signals and determine synaptic summation modes.

Understanding how ionic currents shape membrane temporal properties is essential for dendritic computation, influencing whether dendrites function as integrators or coincidence detectors. This paper explores the effects of A-type potassium, T-type calcium, and transient sodium currents on synaptic temporal summation *in vivo*-like conditions, focusing on their impact on voltage traces and summation properties (integrator vs. coincidence detector).

Results

Consistent membrane charging effects in the presence of potassium and sodium currents, but mixed response effects in the presence of calcium current

We begin our paper testing the effect of inactivating currents on τ_m. For that, we built a single compartment dendritic model. We focused on the most relevant inactivating currents expressed in pyramidal neurons dendrites and activated near the spiking threshold: A-type potassium (I_{KA}), T-type calcium (I_{CaT}), and transient sodium (I_{NaT}) (see Methods). A depolarizing pulse of current was applied, and both exponential rise and decay followed by this pulse were analyzed. Fig. 1A shows that I_{KA} hyperpolarizes the resting membrane potential, reduces the amplitude of the response, and accelerates the capacitor's charge. In contrast, I_{NaT} amplifies the response

amplitude and slows down the capacitor's charge but has no effect on the resting membrane potential due to its activation at higher membrane potentials (Fig 1B).

Opposed to this pattern, the effects of I_{CaT} were mixed. I_{CaT} depolarizes the resting membrane potential. However, there is only amplification of the voltage change at the onset of the current pulse, while there is a reduction of the voltage change at the end of the pulse due to slow inactivation kinetics (Fig 1C). We also observed a clear phase delay during the rising phase of the EPSP (excitatory postsynaptic potential), but the decay phase showed mixed behavior, starting with a phase delay in one direction and eventually reversing its direction (Fig 1D). We believe this mixed behavior in amplification/reduction of the voltage change and lengthening/shortening of the voltage provides insight into the inconsistent reports found in the literature about I_{CaT} (Stuart et al. 1995; González-Burgos et al. 2001; Andreasen et al. 1999; Hsu et al. 2018; Seong et al. 2014, Fukaya et al. 2018; Gillessen et al. 1997, Prescott et al. 2005, Liu et al. 2008; Connelly et al. 2016; Urban et al. 1998; Evans et al. 2017; Deleuze et al. 2012).

Voltage changes scaling monotonically during theta oscillations

The previous section studied the effect of the inactivating currents on the temporal properties of a dendritic model. The model was stimulated using simple current pulses and simulated EPSPs. Here, we wondered whether the previous results also apply under *in vivo*-like conditions. Here, we investigated the effects of the inactivating currents on scaling voltage traces from *in vivo*-like conditions. We injected synaptic currents, consisting of evenly distributed EPSCs and IPSCs over time, to generate sparse synaptic backgrounds as found *in vivo* (Waters et al., 2006). To add

realistic background to the synaptic currents, we simulated theta oscillations at 4 Hz and analyzed four cycles of voltage traces (Fig. 2; cycles identified by different colors). Our results show that I_{KA} causes a negative shift of the voltage changes (Fig 2A), whereas I_{CaT} and I_{NaT} cause a positive shift (Fig 2C, 2E). The scaling from above -60 mV is linearly correlated with the membrane voltage for I_{KA} and I_{NaT} (Fig 2B, 2F) but no clear tendency is found for I_{CaT}, only high variability (Fig 2D).

Fig 3 shows the nonlinear scaling for input frequency oscillations from 1 to 30 Hz. The set of Figs 3A-C demonstrate a clear difference in the voltage scaling when comparing the ionic currents. More specifically, we observed a consistent decrease for I_{KA} across depolarizing voltages and a consistent increase for I_{NaT} across depolarizing voltages (see heatmaps in Fig 3D and Fig 3F). In contrast, I_{CaT} showed nonmonotonic behavior of the scaling for low frequencies, but monotonic for high frequencies (Fig 3E). Then we evaluated the behavior of the scaling for different conductance values at 4 Hz. We observed a consistent decrease for I_{KA} across depolarizing voltages and a consistent increase for I_{NaT} across depolarizing voltages (Fig 3G and Fig 3I). In contrast, I_{CaT} showed similar values across voltage (horizontal lines, Fig 3H).

These results suggest that most of the knowledge from the Fig 1 can be transferred to the *in vivo*-like states with except to the I_{CaT}, with ionic currents scaling the voltage differently in a frequency-dependent manner.

138 **Changes in activation are linearly correlated with changes in inactivation for T-type**
139 **calcium and A-type potassium currents**

140 We previously observed the effect of the inactivating currents on the scaling of the voltage. I_{KA}
141 and I_{NaT} showed linear correlation with voltage, but no consistent tendency was observed for
142 I_{CaT}. In this section, to investigate the biophysical mechanisms underlying these discrepancies we
143 present phase plots of activation versus inactivation variables for theta oscillations (Fig. 4). This
144 analysis demonstrated a clear negative correlation, where increases in activation correspond with
145 decreases in inactivation (Fig 4G, 4H, 4J and 4K). Interestingly, the window current properties of
146 I_{NaT} are markedly different than I_{KA} and I_{CaT} and produced a highly nonlinear correlation
147 between activation and inactivation variables, where large values of one variable correlate with
148 small values of the other (Fig 4I). We verified that this relationship is well-fitted by a power law
149 function (Fig 4L).

150

151 Analysis of the activation vs. inactivation phase plots showed that fitting trajectories of I_{KA} and
152 I_{CaT} by a linear regression returns a curve very similar to the trajectories when $\tau_{act} = \tau_{inact} = 0$ (Fig
153 4J and 4K). This allows us to approximate the functional relationship between activation or
154 inactivation. Therefore, we use the linear regression to substitute the inactivation variable by a
155 linear function dependent on the activation variable: $q_{Inact} = - p_{Act} + 0.85$ for I_{KA} and, $q_{Inact} = -$
156 $0.84p_{Act} + 0.8$ for I_{CaT}. In contrast, the trajectories for I_{NaT} are highly nonlinear and, as explained
157 above, were fitted using a power law function with 4/3 exponent ($q_{Inact} = 10^{-3} {p_{Act}}^{-4/3}$) (Fig 4I
158 and 4L). This functional behavior is the result of the way activation and inactivation curves
159 interact within the window current.

160

161 Our results showed similar activation/inactivation linear trajectories for I_{KA} and I_{CaT}, although
162 these two currents differ in their inactivation kinetics (e.g. τ_{inact} = 5 ms for I_{KA} but 10 ms for I_{CaT}).
163 This suggests that under *in vivo*-like conditions, voltage changes are robust to inactivation
164 kinetics.
165
166
167 **Slow inactivation plays nearly no role on summation during *in vivo*-like states**
168 Based on the results above, we interrogate whether *in vivo*-like states require kinetics. Therefore,
169 we investigated whether we could get similar voltage traces when using the actual kinetics vs.
170 when using fast kinetics, i.e. $\tau_{act} = \tau_{inact}$ = 0.1 ms. Surprisingly, for all simulated currents we
171 obtained traces that were similar with average differences less than 0.6 mV for voltages below
172 spiking threshold (V = -40 mV; Fig 5D). These results suggest that the system of equations can
173 be reduced when assuming $\tau_{act} = \tau_{inact}$ = 0, hinting that the dynamics provided by Eq 3 is no
174 longer necessary for *in vivo*-like conditions. Suprathreshold spiking activity also displayed
175 similar results (Suppl Fig 1).
176
177 Further, and following the relationships from the previous section, we can also reduce the
178 inactivation variable using the linear relation obtained from the linear regression above for I_{KA}
179 and I_{CaT} and power law approximation for I_{NaT} inactivation. As a result of all the reductions, we
180 can express the behavior of each current as dependent on only a single activation variable.
181 Therefore, we use the linear regression to substitute the inactivation variable by a linear function
182 dependent on the activation variable for I_{KA} and I_{CaT} and power law approximation for I_{NaT}. We

also consider $\tau_{act} = \tau_{inact} = 0$. Fig 5H demonstrates that this approximation can obtain similar voltage traces with average values below 0.7 mV for all currents.

The results from this section allowed us to reduce the dendrite system of equations to a single variable that resolves the activation variable only. Our approximation is akin to the Morris-Lecar reduction (Izhikevich 2007). However, in our case, the assumption of instantaneous kinetics allows us to avoid coupling differential equation.

In the next set of experiments, we wondered about the dependency of our results with the input frequency. Fig 6 shows the voltage difference between the model with slow kinetics vs. instantaneous for input frequency oscillations from 1 to 30 Hz. We observed a consistent increase for all currents across depolarizing voltages, with values below 0.7 mV for I_{KA}, 1.2 mV for I_{CaT} and 0.35 mV for I_{NaT} (Fig 6D, 6E and 6F). Then we evaluated the voltage difference between the model with slow kinetics vs. instantaneous kinetics for different conductance values with input frequency fixed at 4 Hz. We observed a consistent increase for all currents across depolarizing voltages, with lowest values at conductance close to $g_{KA} = 1$, $g_{CaT} = 0.1$ and $g_{NaT} = 50$ (Fig 6G, 6H and 6I).

These results suggest that the voltage differences between the model with slow kinetics and fast kinetics is independent on the frequency input, but dependent on the voltage. As to the latter, the stronger the depolarization the higher was the voltage difference identified, showcasing that the kinetics becomes more prominent as the voltage gets closer to the threshold of the neuron.

206

207 **Inactivation opposes activation effects on voltage scaling and membrane time constant**

208 We know from above that activation and inactivation have negative correlation, but it is still
209 unknown how this correlation determines the voltage scaling and temporal properties of the
210 voltage traces in the presence of I_{KA}, I_{CaT} and I_{NaT}. On the other hand, it is well known that
211 scaling is inversely related to the input conductance and that the temporal properties are related
212 to the membrane time constant. We first used an analytical approach to determine the opposed
213 effect of the inactivation on voltage scaling and temporal properties compared to activation.
214 When comparing the input conductance for inactivating current (as shown in Eq 8) vs non-
215 inactivating current (as shown in Eq 10), we know from Eq 9 that $p_i^\infty q_i^\infty < p_i^\infty$ and $q_i^\infty \frac{\partial p_i^\infty}{\partial v} +$
216 $p_i^\infty \frac{\partial q_i^\infty}{\partial v} < \frac{\partial p_i^\infty}{\partial v}$. Thus, input conductance of inactivating currents is always smaller compared to
217 the non-inactivating case, suggesting that the effect of inactivation is always to oppose to the
218 activation.

219

220 To test the opposite effects of activation and inactivation, we investigated the temporal
221 summation of a train of 3 EPSPs separated by 10 ms. We tested the effect of the inactivating
222 current and their respective non-inactivating version (Fig 7). The plots show that noninactivating
223 currents enhance the effect compared to their inactivating counterpart. These results suggest that
224 inactivation counteracts the effect of the activation, reducing its effect.

225

226 While in this section we showed that inactivation opposes activation effects on voltage scaling
227 and membrane time constant with analytical derivations, together with previous sections we can
228 conclude that I_{KA} activation shortens τ_m whereas inactivation prolongs it (Fig 7A). Meanwhile,

229 an opposite effect occurs for I_{CaT} and I_{NaT} (Fig 7B and 7C). Together, these observations have
230 profound implications for dendritic computation, in particular to their temporal summation
231 properties. In the next section, we will show how our results are useful to study synchrony- vs.
232 rate-code.
233
234
235 **A-type potassium current enhances synchrony-code but T-type calcium and transient**
236 **sodium currents enhance rate-code**
237 Temporal summation of synaptic potentials can be used to identify integrators or coincidence
238 detector neurons. Integrators, characterized by a long τ_m, allow summation of synaptic potentials
239 even when they occur far apart in time. In contrast, coincidence detectors, with a short τ_m,
240 integrate synaptic potentials only when they occur closely together in time. Previous studies have
241 shown the association between high expression of potassium currents and coincidence detection
242 mode, and high expression of calcium/sodium currents and integration mode (Mathews et al
243 2010, Branco et al. 2016). We tested this hypothesis using an analytical approach to demonstrate
244 that for instantaneous inactivating currents, potassium currents such as I_{KA} always decrease the
245 input resistance and shorten the membrane time constant, meanwhile calcium/sodium currents
246 such as I_{CaT}, and I_{NaT} always increase the input resistance and prolong the membrane time
247 constant (see Methods, section Mathematical analysis of reducing/contracting and
248 amplifying/prolonging currents).
249
250 Moreover, coincidence detection and integration on the level of dendritic compartments can be
251 seem translated to synchrony-code and rate-code on the level of network computations, with

coincidence detectors being more likely to fire with synchronized inputs and poorly integrate sparse inputs. In contrast, integrators can summate sparse inputs to generate dendritic spikes but respond less to coincident inputs compared to coincidence detectors. Thus, a natural question we investigate in this section is how the modulation of the I_{KA}, I_{CaT} and I_{NaT} affect the synchrony vs. rate-code.

Accordingly, we randomly generated 100 sparse and 100 synchronous input currents and used them to generate 100 voltage traces also stimulated by theta input (4 Hz). The sparse and synchronous input were developed to create distinction between these codes (synchrony- vs. rate-code). Both sparse and synchronous inputs had the same amount of 200 EPSCs and 200 IPSCs randomly distributed in the course of a simulation. For the synchronous case, we removed randomly 75% of the EPSCs and the remaining were amplified by a factor of 4 with the rationale of reproducing a highly synchronous set of inputs although sparse.

While a consistent decrease in firing occurs in the presence of the I_{KA} (compare Fig 8A to B), an increase in firing occurs for I_{CaT} and I_{NaT} (compare Fig 8A to C and D). This aligns with the shrinkage and amplification of voltage changes seen above. When all three currents were present, firing rates remained unchanged (not shown), indicating that the effects of I_{KA} were counteracted by I_{CaT} and I_{NaT} as expected.

To further quantify our results in Fig. 8, we require a metric that can determine the preferred synaptic summation mode (coincidence vs. integration). Thus, we calculated the relative change in spiking frequency of a dendrite when presented with sparse versus synchronized synaptic

inputs. We expect that coincidence detectors will show an increase in relative spiking frequency, while integrators will show a decrease. We tested this new metric in a single passive compartment dendrite model by changing the conductance value or capacitance density (Suppl Fig 2). The heatmap shows the percentage of relative frequency change when dendrites were stimulated using sparse vs synchrony input. We used this index (% relat freq) as a measure of the strength of the preferred neural code mode employed by the dendrite. For instance, % relat freq of 100% suggests the dendrite acts as a perfect coincident detector, meanwhile 0% suggests the dendrite acts as a perfect integrator. According to the values obtained from the index, we found that the dendrite would act closer to a perfect integrator when g_{Leak} was low or when capacitance density was high, both conditions consistent with long τ_m.

As shown in Fig 8, synchronous input increases firing rate. The relative increase in frequency is highest at the onset of the rise and decay of the theta cycle and lowest at the peak (Fig 8E, 8F, 8G and 8H). The exception is the potassium current where no large relative increase was observed at the decay (Fig 8F). We also calculated the relative difference of frequency between sparse vs synchronous stimulation (Fig 8E, 8F, 8G and 8H). We found a significant increase in the presence of I_{KA} relative to the passive dendrite (17.44 ± 1.38 % for passive, 38.86 ± 4.65 % for I_{KA}, $p < 0.001$). We also found a significant decrease in the presence of I_{CaT} and I_{NaT} relative to the passive dendrite (9.77 ± 0.81 % for I_{CaT}, 10.53 ± 0.8 % for I_{NaT}, $p < 0.001$). Also, I_{KA} was significantly higher than I_{CaT} and I_{NaT} ($p<0.001$). Finally, I_{CaT} and I_{NaT} were not significantly different ($p = 0.5$). These results suggest that I_{KA} enhances synchrony-code, but I_{CaT} and I_{NaT} enhance rate-code.

298 We then expand our analysis to investigate the tuning range of specific neural code modes and
299 how they depend on the conductance values of I_{KA}, I_{CaT} and I_{NaT}. We use the same dendritic
300 model used above, but now we added all 3 currents to the model, while changing their
301 conductance values selectively. According to the values obtained from the index, we found that
302 the dendrite would act closer to a perfect integrator when g_{KA} was low (Fig 9C) or when
303 g_{CaT}/g_{NaT} were high (Fig 9G, H). Under these conditions, the variability of the other
304 conductances did not affect much the index value (the heatmaps are blueish). These results
305 suggest I_{KA} is responsible for changing the dendrite to a more coincidence detection mode
306 meanwhile I_{CaT} and I_{NaT} take the dendrite closer to an integration mode. This can also be
307 observed for high values of g_{KA} (see Fig 9I) or when g_{CaT}/g_{NaT} is low (Fig 9A, B). Under these
308 conditions the variability of the other conductances play a significant role that affects the index
309 value (the heatmaps change from dark blue to light yellow).
310
311
312 **Discussion**
313 This study examines an important aspect of the neural coding by focusing on different modes of
314 *in vivo* dendritic synaptic integration. We show the role of inactivating currents on dendritic
315 temporal properties, and how the modes vary from integration of synaptic potentials over time
316 (long τ_m) to coincidence detection of closely timed potentials (short τ_m) (Mathews et al. 2010,
317 Prescott and De Koninck 2005, Ceballos et al. 2018, Farries et al. 2010, Branco et al. 2016).
318
319 Our results point to the role of A-type potassium currents in shortening τ_m, while T-type calcium
320 and transient sodium currents lengthen it, similar to non-inactivating currents. This suggests

321 inactivation reduces current strength without altering its profile. Additionally, activation and
322 inactivation affect τ_m in opposite ways, with currents that shorten τ_m upon activation prolonging
323 it upon inactivation and vice versa, consistent with previous studies (Richardson et al. 2003).
324 These findings also apply to fast-activating, non-inactivating currents, e.g. M-type potassium and
325 persistent sodium currents.
326
327 In terms of firing, we found that A-type potassium currents consistently reduce firing rates,
328 whereas T-type calcium and transient sodium currents increase them. This is due to potassium
329 currents hyperpolarizing the membrane, reducing voltage amplitude, and shortening temporal
330 changes, which decreases excitability. In contrast, calcium and sodium currents depolarize the
331 membrane, enhance voltage amplitude, and extend temporal changes, thereby increasing
332 excitability.
333
334 In relation to the effects of inactivating currents under *in vivo*-like conditions with oscillatory
335 inputs and synaptic fluctuations, both I_{KA} and I_{NaT}, were observed scaling changes above -60
336 mV, showing monotonic trends with variability. The rising and decay phases followed distinct
337 pathways, indicating that these currents differentiate between depolarization and
338 hyperpolarization. No clear trend was found for I_{CaT}, but its amplification pattern remained.
339
340 Activation and inactivation trajectories were linearly correlated for I_{KA} and I_{CaT}, but nonlinear for
341 I_{NaT}, independent of kinetics. Surprisingly, activation/inactivation kinetics had minimal impact
342 on voltage changes, with differences of less than 1 mV, suggesting potential misinterpretations
343 when extrapolating *in vitro* data to *in vivo* contexts. This underscores the importance of *in vivo*

344 recordings to fully understand dendritic behavior (Moore et al. 2017, Ujfalussy et al. 2018,
345 Dembrow et al. 2022, Liao et al. 2024).
346
347 We can regard our results as a step towards understanding how dendrites process information. In
348 particular, we have also tested temporally distinct patterns. Synaptic summation in the presence
349 of A-type potassium currents promoted firing with synchronized input, while T-type calcium and
350 transient sodium currents supported firing with sparse input. Thus, A-type potassium currents
351 enhance synchrony-coding, whereas calcium and sodium currents favor rate-coding. These
352 currents modulate dendritic integration in cortical and hippocampal dendrites (Stuart et al.,
353 2015). Our findings align with experimental evidence showing that inactivating T-type calcium
354 currents extend synaptic potentials (Connelly et al. 2016; Gillessen and Alzheimer 1997; Liu and
355 Shipley 2008; Prescott and De Koninck 2005; Urban et al. 1998), and inactivating A-type
356 potassium channels shorten them (Hoffman et al. 1997; Mathews et al. 2010). Notably, we are
357 the first to show that transient sodium currents have a lengthening effect.
358
359 Future work should explore other factors influencing the activation/inactivation properties of
360 ionic currents and systematize findings across species. For example, sodium and potassium
361 current voltage-dependence is more depolarized in humans than mice (Wilbers, 2023), and
362 isoflurane hyperpolarizes sodium current inactivation (Qiu et al., 2023). Neuromodulation also
363 enhances sodium current inactivation (Chen et al., 2006). Though we focus on *in vivo*-like states,
364 future studies could investigate how alternating states affect synaptic integration.
365
366

Methods

Dendrite model

The most general case of a Hodgkin-Huxley (HH) current involves two gating variables: p for activation and q for inactivation. This type of current is referred to as "inactivating" and acts as a break to close the channel (Hille, 2001). Each gating process has its own time constant, denoted as τ_{act} for activation and τ_{inact} for inactivation.

The current equation is

$$C\frac{dv}{dt} = \sum_{i=1}^{n} I_i(v) + I_{inj}, \qquad \text{(Eq 1)}$$

where C is the capacitance, v is the voltage, $I_i(v)$ is the voltage-dependent current, n is the number of ionic currents and I_{inj} is the injected current. In our paper, ionic currents will be represented using the HH formalism:

$$I_i = \bar{g}_i p_i q_i \left(V - E_{rev}^{i}\right), \qquad \text{(Eq 2)}$$

where $\bar{g}_i$ is the maximum conductance, E_{rev}^{i} the reversal potential, and for (x=p,q) we have

$$\frac{dx}{dt} = \frac{x^{\infty} - x}{\tau_{act/inact}}. \qquad \text{(Eq 3)}$$

In Eq. 3, x^{∞} is the steady-state activation variable and it is represented by a sigmoid function following

$$x^{\infty}(v) = \frac{1}{1+e^{\left(\frac{V-V_{1/2}}{-k}\right)}}. \qquad \text{(Eq 4)}$$

Where $V_{1/2}$ and k are constants. Importantly, $p = p(v,t)$ and $q = q(v,t)$, i.e., activation and inactivation variables are dependent on voltage and time.

In this paper we only address inactivating currents activated by depolarization such as transient sodium, A-type potassium and T-type calcium. One important mathematical property of p and q in this situation that can be derived from the fact that they are activation and inactivation functions is that $\frac{\partial p}{\partial v} > 0$ and $\frac{\partial q}{\partial v} < 0$, although $p > 0$ and $q > 0$. This behavior occurs for currents activated by depolarization, opposed to when the currents are activated by hyperpolarization ($\frac{\partial p}{\partial v} < 0$ and $\frac{\partial q}{\partial v} > 0$).

Importantly, many inactivating potassium, sodium, and calcium currents follow Equation 2, while some variations of this equation exist where the activation or inactivation variables are raised to an exponent (such as 2, 3 or 4). Thus, the equation can be represented as $I_i = \bar{g}_i {p_i}^x {q_i}^y (V - E^i_{rev})$. Although we will use this representation in our simulations, we will use the simple version as shown in Eq.2 for the analytical approximation.

We performed computer simulations using custom-made codes in Matlab. A single compartment dendritic model with ionic currents using the HH formalism. Three types of currents were

412 investigated: A-type potassium, T-type calcium and transient sodium. Capacitance density was
413 1μF/cm^2. Activation variables were defined by the following parameters: for potassium: $V_{1/2}$ = -
414 50 mV, k = 15, for calcium: $V_{1/2}$ = -50 mV, k = 15, and for sodium: $V_{1/2}$ = -30 mV, k = 5.
415 Inactivation variables were defined by the following parameters: for potassium: $V_{1/2}$ = -60, k =
416 15, for calcium: $V_{1/2}$ = -60 mV, k = 15, and for sodium: $V_{1/2}$ = -60 mV, k = 5. Activation kinetics
417 was τ_{act} = 0.2, 0.5 and 0.05 ms for potassium, calcium and sodium respectively. Inactivation
418 kinetics was τ_{inact} = 5, 10 and 0.5 ms for potassium, calcium and sodium respectively.
419 Conductance densities were expressed as mS/cm^2 with values: g_K = 1, g_{Ca} = 0.1 and g_{Na} = 50.
420 Leak conductance density was 0.3 mS/cm^2. Reversal potential was E_{rev} = -80, 50 and 50 mV, for
421 potassium, calcium and sodium respectively. Leak conductance reversal potentials was -80 mV.
422
423 Models of A-type potassium, T-type calcium and transient sodium currents are a modified
424 version from Engbers et al 2012, Jaffe et al 1994, Korngreen et al 2000, Dougalis et al 2017, and
425 Hoffman et al. 1997. A-type potassium current equation is: $I_{kA} = g_{ak} n_{ka}^4 l_{ka}(E_K - V)$. T-type
426 calcium current equation is: $I_{CaT} = g_{CaT} {m_{CaT}}^2 h_{CaT}(E_{Ca} - V)$. Transient sodium current
427 equation is: $I_{NaT} = g_{Na} m_{Na}^2 h_{Na}(E_{Na} - V)$. Leak current equation is: $I_L = g_L(E_L - V)$.
428
429
430 **Simulations**
431 Differential equations were solved using the Euler method and time step 0.05 ms. Synaptic
432 background activity was generated of evenly distributed excitatory postsynaptic currents
433 (EPSCs) and inhibitory postsynaptic currents (IPSCs) over time, to generate sparse synaptic
434 backgrounds as found *in vivo* (Waters et al., 2006). EPSCs and IPSCs were generated using

435 biexponential events: V_{Hold} = -50 mV, E_{AMPA} = 0 mV, E_{GABAA} = -60 mV and g = 0.1 nS. The time

436 constants are $\tau_{rise/AMPA}$ = 1 ms, $\tau_{decay/AMPA}$ = 10 ms, $\tau_{rise/GABAA}$ = 2 ms, $\tau_{decay/AMPA}$ = 20 ms.

437

438 We simulated theta oscillations at 4 Hz and analyzed four cycles of voltage traces. We generated

439 dendritic spikes using a leaky-integrate and fire model with resting potential -60 mV and spiking

440 threshold -40 mV.

441

442

443 **Mathematical analysis of reducing/contracting and amplifying/prolonging currents**

444 Here we used an analytical approach to determine the effect of I_{KA}, I_{CaT}, and I_{NaT} on the input

445 resistance and membrane time constant. It is well known that τ_m is a function of I_i:

446 $$\tau_m = \frac{C}{\sum_{i=1}^{n} G_i}, \qquad \text{(Eq 5)}$$

447

448 where the input conductance G_i can be obtained by differentiating Eq.2:

449

450 $$G_i = \frac{\partial I_i}{\partial v} = \bar{g} p_i q_i + \bar{g}(V-E) q_i \frac{\partial p_i}{\partial v} + \bar{g}(V-E) p_i \frac{\partial q_i}{\partial v}. \qquad \text{(Eq 6)}$$

451

452 As discussed in the methods section, in this study all currents are inactivating. As shown in the

453 results section (see Slow inactivation plays nearly no role on summation during *in vivo*-like

454 states allowing for model reduction), all the inactivating currents produce similar voltage

455 changes when it is assumed fast activation/inactivation kinetics. Under these circumstances, it is

456 reasonable to assume $\tau_{act} = \tau_{inact} \rightarrow 0$. Consequently, p and q become functions of voltage alone,

457 denoted as p = p(V) and q = q(V). In this state, they lose their time dependence and are solely

voltage dependent. Specifically, $p = p^{\infty}(v)$ and $q = q^{\infty}(v)$. Therefore, when $\tau_{act} = \tau_{inact} \rightarrow 0$, Eq 6 can be expressed as:

$$\frac{\partial I_i}{\partial v} = \bar{g} p_i^{\infty} q_i^{\infty} + \bar{g}(V - E) q_i^{\infty} \frac{\partial p_i^{\infty}}{\partial v} + \bar{g}(V - E) p_i^{\infty} \frac{\partial q_i^{\infty}}{\partial v} \qquad \text{(Eq 7)}$$

$$\frac{\partial I_i}{\partial v} = \bar{g} p_i^{\infty} q_i^{\infty} + \bar{g}(V - E)\left(q_i^{\infty} \frac{\partial p_i^{\infty}}{\partial v} + p_i^{\infty} \frac{\partial q_i^{\infty}}{\partial v}\right). \qquad \text{(Eq 8)}$$

The term $\alpha = (V - E)\left(q_i^{\infty} \frac{\partial p_i^{\infty}}{\partial v} + p_i^{\infty} \frac{\partial q_i^{\infty}}{\partial v}\right)$ can assume positive or negative values. According to Eq. 5, when $\alpha > 0$, τ_m decreases and voltage changes are reduced, whereas when $\alpha < 0$, τ_m increases, and voltage changes are amplified. Currents with negative α are termed "amplifying/prolonging" as they lengthen τ_m, while those with a positive α are termed "reducing/contracting", as they shorten τ_m (Ceballos et al., 2017b).

The question arises: under what circumstances do the currents "amplify/prolong" or "reduce/contract"? To answer this, we need to investigate the conditions when α is positive or negative. We know that:

$$\frac{\partial p^{\infty}}{\partial v} > 0,\ \frac{\partial q^{\infty}}{\partial v} < 0,\ p^{\infty} > 0, \text{and}\ q^{\infty} > 0. \qquad \text{(Eq 9)}$$

Therefore, $q_i^{\infty} \frac{\partial p_i^{\infty}}{\partial v}$ is positive and $p_i^{\infty} \frac{\partial q_i^{\infty}}{\partial v}$ is negative. We also know that the membrane potential of dendrites typically ranges between -90 mV and +60 mV. The reversal potential for potassium (E_k) is usually assumed to be around -90 mV, while the reversal potential for sodium and

calcium ($E_{Na,Ca}$) is assumed to be around +60 mV. Thus, for I_K ocurrs $V - E_k > 0$. Similarly, for I_{CaT} and I_{NaT}, V- $E_{Na,Ca}$ <0.

Substituting these into Eq. 7, we find that for I_K the first term is positive, the second is positive and the third is negative. Meanwhile, for I_{CaT} and I_{NaT}, the second is negative and the third is positive. This demonstrates that activation and inactivation have opposite effects on τ_m: one prolongs it while the other shortens it. This observation is consistent with the findings of Remme et al. (2011) and Richardson et al. (2003) that I_{KA} activation reduces, and inactivation amplifies the voltage scaling, and that I_{KA} activation shortens, and inactivation prolongs τ_m. Meanwhile, the opposite effect occurs for I_{CaT} and I_{NaT}.

A special case arises when inactivation is removed. This occurs for some voltage-dependent currents that exhibit either no inactivation or very slow inactivation (also known as nonactivating currents). This scenario can be simulated by setting q = 1. Therefore, we ask: when can $\alpha = (V - E)\frac{\partial p_i^\infty}{\partial v}$ be positive or negative, i.e., when does it contract or prolong τ_m, after inactivation is removed? We can easily deduce that, $(V - E_k)\frac{\partial p_i^\infty}{\partial v} > 0$ but $\left(V - E_{Na,Ca}\right)\frac{\partial p_i^\infty}{\partial v} < 0$. This suggests that when removing the inactivation from I_{KA}, α is positive i.e., it is always a "contracting" current, meanwhile for I_{CaT} and I_{NaT} , α is negative i.e., it is always a "prolonging" current.

Reduction of dendritic model

Here, we show how we approximated I_{KA}, I_{CaT}, and I_{NaT} to polynomial functions of the voltage. Our results suggest that under *in vivo*-like conditions, where the dendritic model receives theta oscillations and synaptic background noise, activation and inactivation variables can be simplified to a combination of polynomial functions. This derives from the observation that phase plots reveal inactivation variable of I_{KA} negatively correlated with its activation variable, and the same for I_{CaT}, allowing the reduction of these two variables into one. Similarly, sodium inactivation variable follows a power law with a 4/3 exponent of the activation variable.

Based on these findings, we propose a reduced model in which subthreshold activity is governed by the approximated dynamics of the HH currents (I_{KA}, I_{CaT}, and I_{NaT}), while suprathreshold activity is modeled by a fire-and-reset rule, i.e. integrate-and-fire model, which we assume as having a threshold at -40 mV. To recapitulate, we modeled the currents using HH formalism, where A-type potassium current equation $I_{kA} = g_{ak} n_{ka}^4 l_{ka}(E_K - V)$, T-type calcium current equation $I_{CaT} = g_{CaT} {m_{CaT}}^2 h_{CaT}(E_{Ca} - V)$, transient sodium current equation $I_{NaT} = g_{Na} m_{Na}^2 h_{Na}(E_{Na} - V)$, and leak current equation $I_L = g_L(E_L - V)$. When we apply all the approximations, I_{KA} is expressed as a 6th order polynomial of the voltage

$$I_{KA} = g_{kA}(aV^5 + bV^4 + cV^3 + dV^2 + eV + f)(E_K - V), \qquad \text{(Eq. 11)}$$

I_{CaT} as a 5th order polynomial of the voltage

$$I_{CaT} = g_{CaT}(aV^4 + bV^3 + cV^2 + dV + e)(E_{Ca} - V), \qquad \text{(Eq. 12)}$$

and I_{NaT} as a power law

$$I_{NaT} = g_{Na} m_{Na}^2 k m_{Na}^{-4/3} (E_{Na} - V) = g_{Na} k m_{Na}^{2/3} (E_{Na} - V)$$

$$= g_{Na} (aV^3 + bV^2 + cV + c)^{2/3} (E_{Na} - V) \qquad \text{(Eq. 13)}$$

The currents I_{KA} and I_{CaT} can be added in a single 6th order polynomial of the voltage. The key advantage of this approach is that it allows this equation alone to fully determine the dendrite's voltage dynamics during *in vivo*-like conditions:

$$C \frac{dv}{dt} = I_{KA} + I_{CaT} + I_{NaT} + I_L. \qquad \text{(Eq. 14)}$$

We call this dendritic model as 6th degree polynomial integrate-and-fire (SIF).

References

1. Remme, M. W., & Rinzel, J. (2011). Role of active dendritic conductances in subthreshold input integration. Journal of computational neuroscience, 31, 13-30.

2. Ceballos, C. C., Roque, A. C., & Leão, R. M. (2017a). The role of negative conductances in neuronal subthreshold properties and synaptic integration. Biophysical reviews, 9, 827-834.

3. Ceballos, C. C., Roque, A. C., & Leao, R. M. (2017b). A negative slope conductance of the persistent sodium current prolongs subthreshold depolarizations. Biophysical Journal, 113(10), 2207-2217.

4. Ceballos, C. C., Pena, R. F., Roque, A. C., & Leão, R. M. (2018). Non-Decaying postsynaptic potentials and delayed spikes in hippocampal pyramidal neurons generated by a zero slope conductance created by the persistent Na+ current. Channels, 12(1), 81-88.

5. Richardson, M. J., Brunel, N., & Hakim, V. (2003). From subthreshold to firing-rate resonance. Journal of neurophysiology, 89(5), 2538-2554.

6. Liu S, Shipley MT (2008) Intrinsic conductances actively shape excitatory and inhibitory postsynaptic responses in olfactory bulb external tufted cells. J Neurosci 28:10311–10322

7. Prescott SA, De Koninck Y (2005) Integration time in a subset of spinal lamina I neurons is lengthened by sodium and calcium currents acting synergistically to prolong subthreshold depolarization. J Neurosci 25:4743–4754

8. Hoffman DA, Magee JC, Colbert CM, Johnston D (1997) K+ channel regulation of signal propagation in dendrites of hippocampal pyramidal neurons. Nature 387:869–875

9. Mathews PJ, Jercog PE, Rinzel J, Scott LL, Golding NL (2010) Control of submillisecond synaptic timing in binaural coincidence detectors by Kv1 channels. Nat Neurosci 13:601–609

10. Farries MA, Kita H, Wilson CJ (2010) Dynamic spike threshold and zero membrane slope conductance shape the response of subthalamic neurons to cortical input. J Neurosci 30:13180–13191

11. Branco T, Tozer A, Magnus CJ, Sugino K, Tanaka S, Lee AK, Wood JN, Sternson SM (2016) Near-perfect synaptic integration by Na v 1.7 in hypothalamic neurons regulates body weight. Cell 165:1749–1761

12. Carter, B. C., Giessel, A. J., Sabatini, B. L., & Bean, B. P. (2012). Transient sodium current at subthreshold voltages: activation by EPSP waveforms. Neuron, 75(6), 1081-1093.

13. González-Burgos, G., & Barrionuevo, G. (2001). Voltage-gated sodium channels shape subthreshold EPSPs in layer 5 pyramidal neurons from rat prefrontal cortex. Journal of Neurophysiology, 86(4), 1671-1684.

14. Deleuze, C., David, F., Béhuret, S., Sadoc, G., Shin, H. S., Uebele, V. N., ... & Bal, T. (2012). T-type calcium channels consolidate tonic action potential output of thalamic neurons to neocortex. Journal of Neuroscience, 32(35), 12228-12236.

15. Rudolph, M., & Destexhe, A. (2003). Tuning neocortical pyramidal neurons between integrators and coincidence detectors. Journal of computational neuroscience, 14, 239-251.

16. Brette, R. (2015). Philosophy of the spike: rate-based vs. spike-based theories of the brain. Frontiers in systems neuroscience, 9, 140675.

17. Hong, S., Ratté, S., Prescott, S. A., & De Schutter, E. (2012). Single neuron firing properties impact correlation-based population coding. Journal of Neuroscience, 32(4), 1413-1428.

18. Azouz, R., & Gray, C. M. (2000). Dynamic spike threshold reveals a mechanism for synaptic coincidence detection in cortical neurons in vivo. Proceedings of the National Academy of Sciences, 97(14), 8110-8115.

19. Wilbers, R., Metodieva, V. D., Duverdin, S., Heyer, D. B., Galakhova, A. A., Mertens, E. J., ... & Goriounova, N. A. (2023). Human voltage-gated Na+ and K+ channel properties underlie sustained fast AP signaling. Science advances, 9(41), eade3300.

20. Qiu, J., Yang, Y., Liu, J., Zhao, W., Li, Q., Zhu, T., ... & Zhou, C. (2023). The volatile anesthetic isoflurane differentially inhibits voltage-gated sodium channel currents between pyramidal and parvalbumin neurons in the prefrontal cortex. Frontiers in Neural Circuits, 17, 1185095.

21. Chen, Y., Frank, H. Y., Surmeier, D. J., Scheuer, T., & Catterall, W. A. (2006). Neuromodulation of Na+ channel slow inactivation via cAMP-dependent protein kinase and protein kinase C. Neuron, 49(3), 409-420.

22. Fukaya, R., Yamada, R., & Kuba, H. (2018). Tonotopic variation of the T-type Ca2+ current in avian auditory coincidence detector neurons. Journal of Neuroscience, 38(2), 335-346.

23. Waters, J., & Helmchen, F. (2006). Background synaptic activity is sparse in neocortex. Journal of Neuroscience, 26(32), 8267-8277.

24. Bourdeau, M. L., Morin, F., Laurent, C. E., Azzi, M., & Lacaille, J. C. (2007). Kv4. 3-mediated A-type K+ currents underlie rhythmic activity in hippocampal interneurons. Journal of Neuroscience, 27(8), 1942-1953.

25. Rathour, R. K., Malik, R., & Narayanan, R. (2016). Transient potassium channels augment degeneracy in hippocampal active dendritic spectral tuning. Scientific reports, 6(1), 24678.

26. Adam, Y., Kim, J. J., Lou, S., Zhao, Y., Xie, M. E., Brinks, D., ... & Cohen, A. E. (2019). Voltage imaging and optogenetics reveal behaviour-dependent changes in hippocampal dynamics. Nature, 569(7756), 413-417.

27. Malezieux, M., Kees, A. L., & Mulle, C. (2020). Theta oscillations coincide with sustained hyperpolarization in CA3 pyramidal cells, underlying decreased firing. Cell Reports, 32(1).

28. Connelly, W. M., Crunelli, V., & Errington, A. C. (2016). Passive synaptic normalization and input synchrony-dependent amplification of cortical feedback in thalamocortical neuron dendrites. Journal of Neuroscience, 36(13), 3735-3754.

29. Gillessen, T., & Alzheimer, C. (1997). Amplification of EPSPs by low Ni2+-and amiloride-sensitive Ca2+ channels in apical dendrites of rat CA1 pyramidal neurons. Journal of neurophysiology, 77(3), 1639-1643.

30. Peng, H., Bian, X. L., Ma, F. C., & Wang, K. W. (2017). Pharmacological modulation of the voltage-gated neuronal Kv7/KCNQ/M-channel alters the intrinsic excitability and synaptic responses of pyramidal neurons in rat prefrontal cortex slices. Acta Pharmacologica Sinica, 38(9), 1248-1256.

31. Urban, N. N., Henze, D. A., & Barrionuevo, G. (1998). Amplification of perforant-path EPSPs in CA3 pyramidal cells by LVA calcium and sodium channels. Journal of Neurophysiology, 80(3), 1558-1561.

32. Stuart, G., & Sakmann, B. (1995). Amplification of EPSPs by axosomatic sodium channels in neocortical pyramidal neurons. Neuron, 15(5), 1065-1076.

33. Andreasen, M., & Lambert, J. D. (1999). Somatic amplification of distally generated subthreshold EPSPs in rat hippocampal pyramidal neurones. The Journal of Physiology, 519(1), 85-100.

34. Evans, R. C., Zhu, M., & Khaliq, Z. M. (2017). Dopamine inhibition differentially controls excitability of substantia nigra dopamine neuron subpopulations through T-type calcium channels. Journal of Neuroscience, 37(13), 3704-3720.

35. Hönigsperger, C., Marosi, M., Murphy, R., & Storm, J. F. (2015). Dorsoventral differences in Kv7/M-current and its impact on resonance, temporal summation and excitability in rat hippocampal pyramidal cells. The Journal of physiology, 593(7), 1551-1580.

36. Hsu, C. L., Zhao, X., Milstein, A. D., & Spruston, N. (2018). Persistent sodium current mediates the steep voltage dependence of spatial coding in hippocampal pyramidal neurons. Neuron, 99(1), 147-162.

37. Hage, T. A., Sun, Y., & Khaliq, Z. M. (2016). Electrical and Ca2+ signaling in dendritic spines of substantia nigra dopaminergic neurons. Elife, 5, e13905.

38. Seong, H. J., Behnia, R., & Carter, A. G. (2014). Impact of subthreshold membrane potential on synaptic responses at dendritic spines of layer 5 pyramidal neurons in the prefrontal cortex. Journal of neurophysiology, 111(10), 1960-1972.

39. Grunditz, Å., Holbro, N., Tian, L., Zuo, Y., & Oertner, T. G. (2008). Spine neck plasticity controls postsynaptic calcium signals through electrical compartmentalization. Journal of Neuroscience, 28(50), 13457-13466.

40. Izhikevich, E. M. (2007). Dynamical systems in neuroscience. MIT press.

41. Prince, L. Y., Tran, M. M., Grey, D., Saad, L., Chasiotis, H., Kwag, J., ... & Richards, B. A. (2021). Neocortical inhibitory interneuron subtypes are differentially attuned to synchrony-and rate-coded information. Communications Biology, 4(1), 935.

42. Hille, B. (2001). Ion Channels of Excitable Membranes Third Edition.

43. Stuart, G. J., & Spruston, N. (2015). Dendritic integration: 60 years of progress. Nature neuroscience, 18(12), 1713-1721.

44. Engbers, J. D., Anderson, D., Asmara, H., Rehak, R., Mehaffey, W. H., Hameed, S., ... & Turner, R. W. (2012). Intermediate conductance calcium-activated potassium channels modulate summation of parallel fiber input in cerebellar Purkinje cells. Proceedings of the National Academy of Sciences, 109(7), 2601-2606.

45. Jaffe, D. B., Ross, W. N., Lisman, J. E., Lasser-Ross, N., Miyakawa, H., & Johnston, D. (1994). A model for dendritic Ca2+ accumulation in hippocampal pyramidal neurons based on fluorescence imaging measurements. Journal of Neurophysiology, 71(3), 1065-1077.

46. Korngreen, A., & Sakmann, B. (2000). Voltage-gated K+ channels in layer 5 neocortical pyramidal neurones from young rats: subtypes and gradients. The Journal of physiology, 525(3), 621-639.

47. Dougalis, A. G., Matthews, G. A., Liss, B., & Ungless, M. A. (2017). Ionic currents influencing spontaneous firing and pacemaker frequency in dopamine neurons of the ventrolateral periaqueductal gray and dorsal raphe nucleus (vlPAG/DRN): A voltage-clamp and computational modelling study. Journal of Computational Neuroscience, 42, 275-305.

48. Moore, J. J., Ravassard, P. M., Ho, D., Acharya, L., Kees, A. L., Vuong, C., & Mehta, M. R. (2017). Dynamics of cortical dendritic membrane potential and spikes in freely behaving rats. Science, 355(6331), eaaj1497.

49. Ujfalussy, B. B., Makara, J. K., Lengyel, M., & Branco, T. (2018). Global and multiplexed dendritic computations under in vivo-like conditions. Neuron, 100(3), 579-592.

50. Dembrow, N. C., & Spain, W. J. (2022). Input rate encoding and gain control in dendrites of neocortical pyramidal neurons. Cell reports, 38(7).

51. Liao, Z., Gonzalez, K. C., Li, D. M., Yang, C. M., Holder, D., McClain, N. E., ... & Negrean, A. (2024). Functional architecture of intracellular oscillations in hippocampal dendrites. Nature Communications, 15(1), 6295.

52. Roome, C. J., & Kuhn, B. (2020). Dendritic coincidence detection in Purkinje neurons of awake mice. elife, 9, e59619.

53. Ratté, S., Hong, S., De Schutter, E., & Prescott, S. A. (2013). Impact of neuronal properties on network coding: roles of spike initiation dynamics and robust synchrony transfer. Neuron, 78(5), 758-772.

54. Stoll, A., Maier, A., Krauss, P., Gerum, R., & Schilling, A. (2023). Coincidence detection and integration behavior in spiking neural networks. *Cognitive Neurodynamics*, 1-13.

55. Dembrow, N. C., Zemelman, B. V., & Johnston, D. (2015). Temporal dynamics of L5 dendrites in medial prefrontal cortex regulate integration versus coincidence detection of afferent inputs. *Journal of Neuroscience*, *35*(11), 4501-4514.

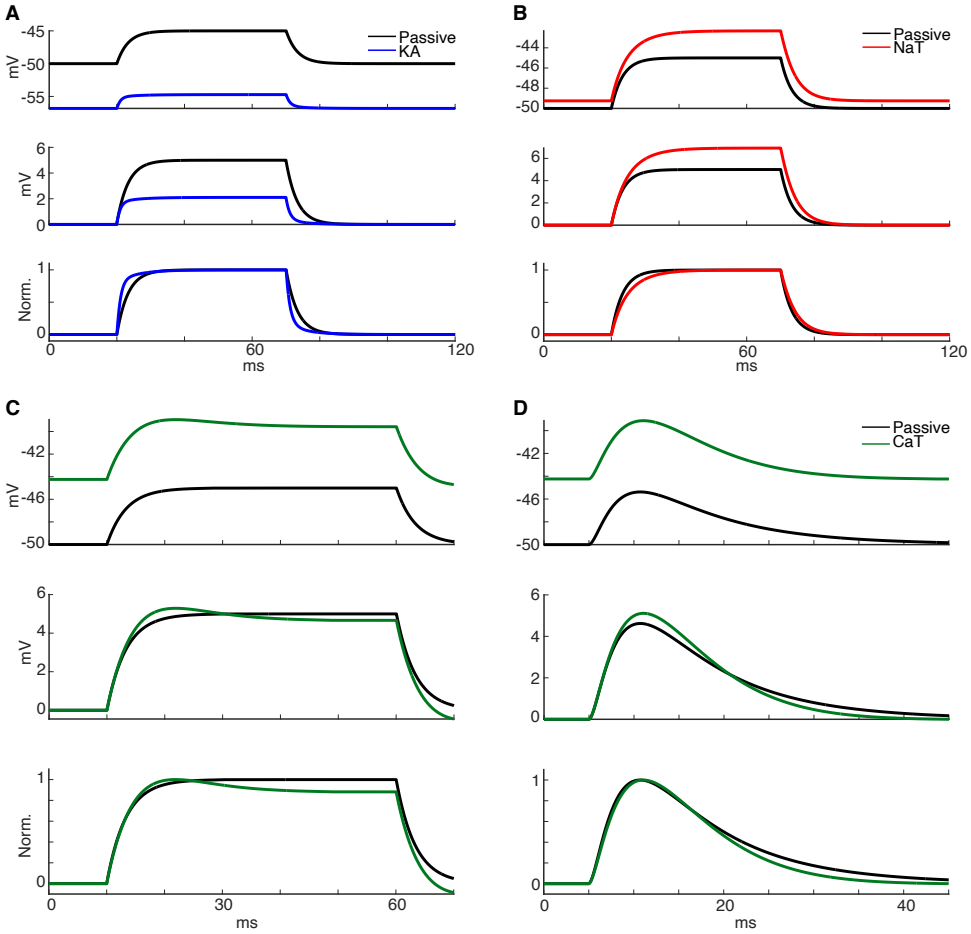

Fig 1. Membrane charging in the presence of the different ionic currents. Each panel has the actual trace with (coloured) and without the current (black) (upper), after baseline subtraction (middle), and after normalization (bottom). A. Constant pulse injected in the presence of I_{KA}. B. Constant pulse injected in the presence of I_{NaT}. C. Constant pulse injected in the presence of I_{CaT}. D. Actual traces of EPSP application, middle: after baseline subtraction, bottom: after normalization. Initial resting membrane potential is -50 mV.

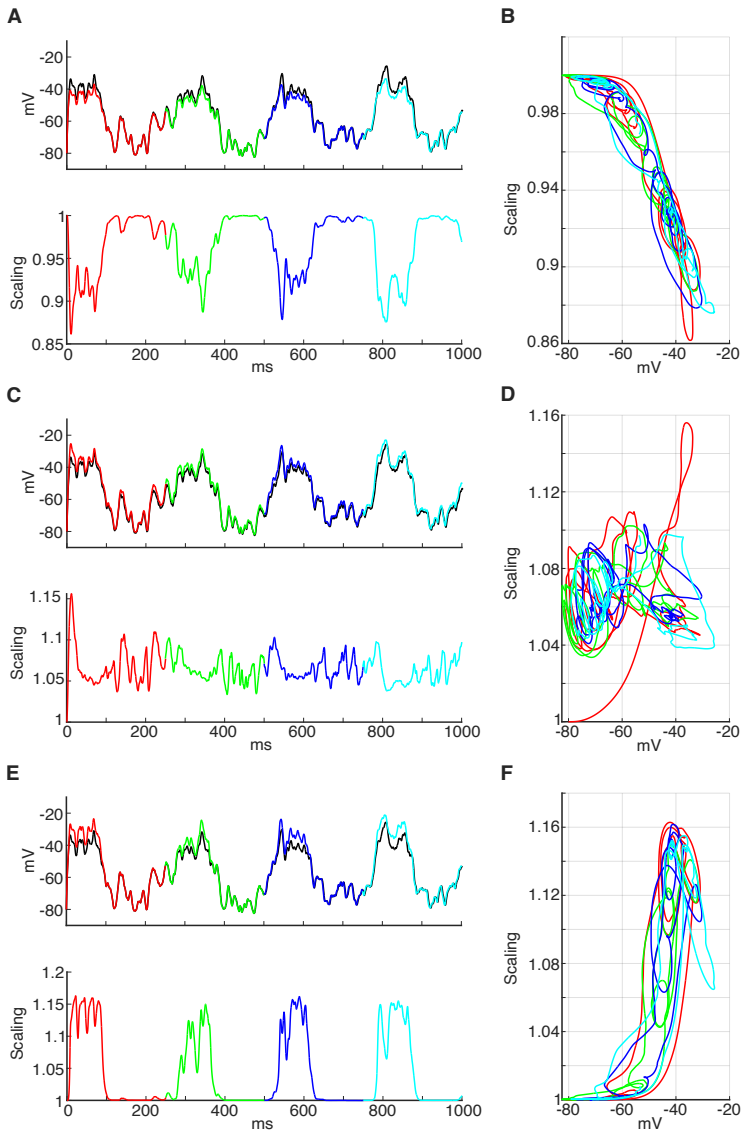

775

776 Fig 2. Voltage changes for dendritic ionic currents under *in vivo*-like conditions. Voltage traces

777 with 4 Hz theta oscillations application and spikes removed. Black solid line: passive dendrite.

778 Red/Green/Blue/Cyan represent first to fourth cycle of the theta sequence with the added ionic

779 current. A. Voltage traces of dendrite expressing only leak current plus I_{KA}. B. phase plot of

780 nonlinear scaling vs membrane potential. C. Voltage traces of dendrite expressing only leak

781 current plus I_{CaT}. D. phase plot of nonlinear scaling vs membrane potential. E. Voltage traces of

782 dendrite expressing only leak current plus I_{NaT}. F. phase plot of nonlinear scaling vs membrane

783 potential.

784

785

786

787

788

789

790

791

792

793

794

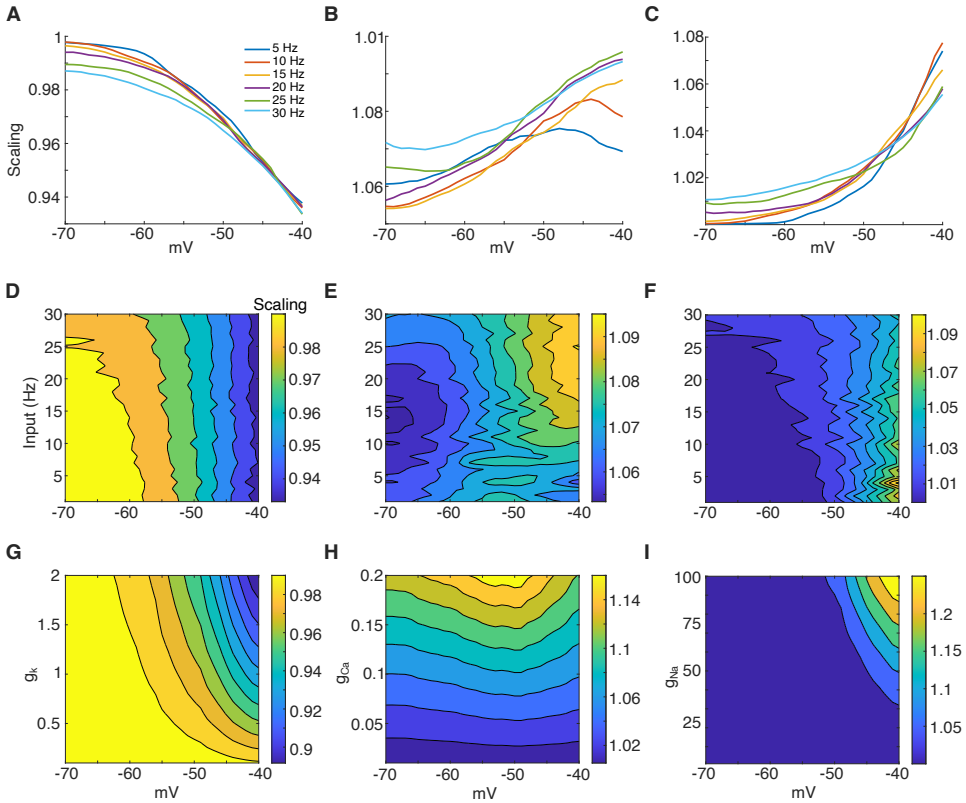

Fig 3. Frequency and ionic effect on voltage scaling. The nonlinear scaling is computed when input frequency oscillations change range from 1 to 30 Hz. A. Curves for added I_{KA}. B. Curves for added I_{CaT}. C. Curves for added I_{NaT}. D. Heatmap of the nonlinear scaling for voltages from -70 to -40 mV vs. input frequency oscillations change from 1 to 30 Hz for I_{KA}. E. Same as in D but for I_{CaT}. F. Same as in D but for I_{NaT}. G. Heatmap of nonlinear scaling for voltages from -70 to -40 mV vs. I_{KA} conductance. E. Same as in G but for I_{CaT} conductance. F. Same as in G but for I_{NaT} conductance.

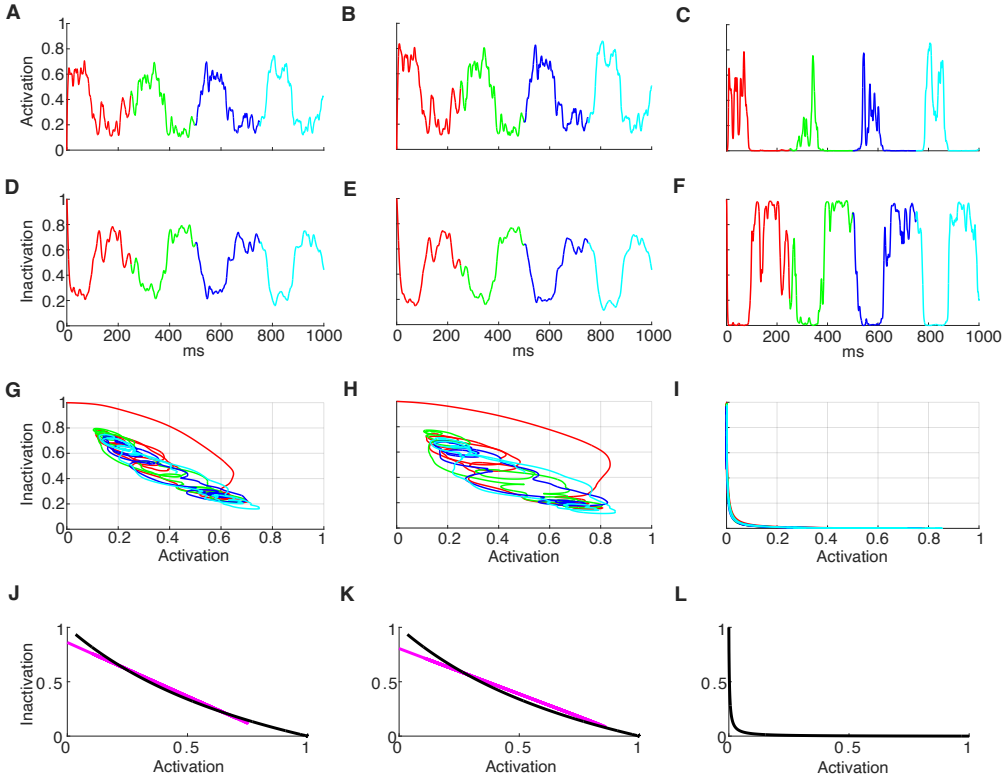

Fig 4. Activation vs. inactivation functional relationships. A-F. The curves represent activation and inactivation variables under 4 Hz theta oscillations. Red/Green/Blue/Cyan represent first to fourth cycle of the theta sequency with the added ionic current: activation for A. I_{KA}. B. I_{CaT}. C. I_{NaT}; inactivation for D. I_{KA}. E. I_{CaT}. F. I_{NaT}. G-I: Phase plots of activation vs inactivation for G. I_{KA}. H. I_{CaT}. I. I_{NaT}. Notice the filtering of the inactivation variable due to the slow inactivation kinetics of I_{CaT} and I_{KA}. J-L: Linear fitting of activation vs. inactivation phase plots for J. I_{KA}. K. I_{CaT} (magenta) and power-law fitting for L. I_{NaT}. Trajectories when $\tau_{act} = \tau_{inact} = 0$ (black).

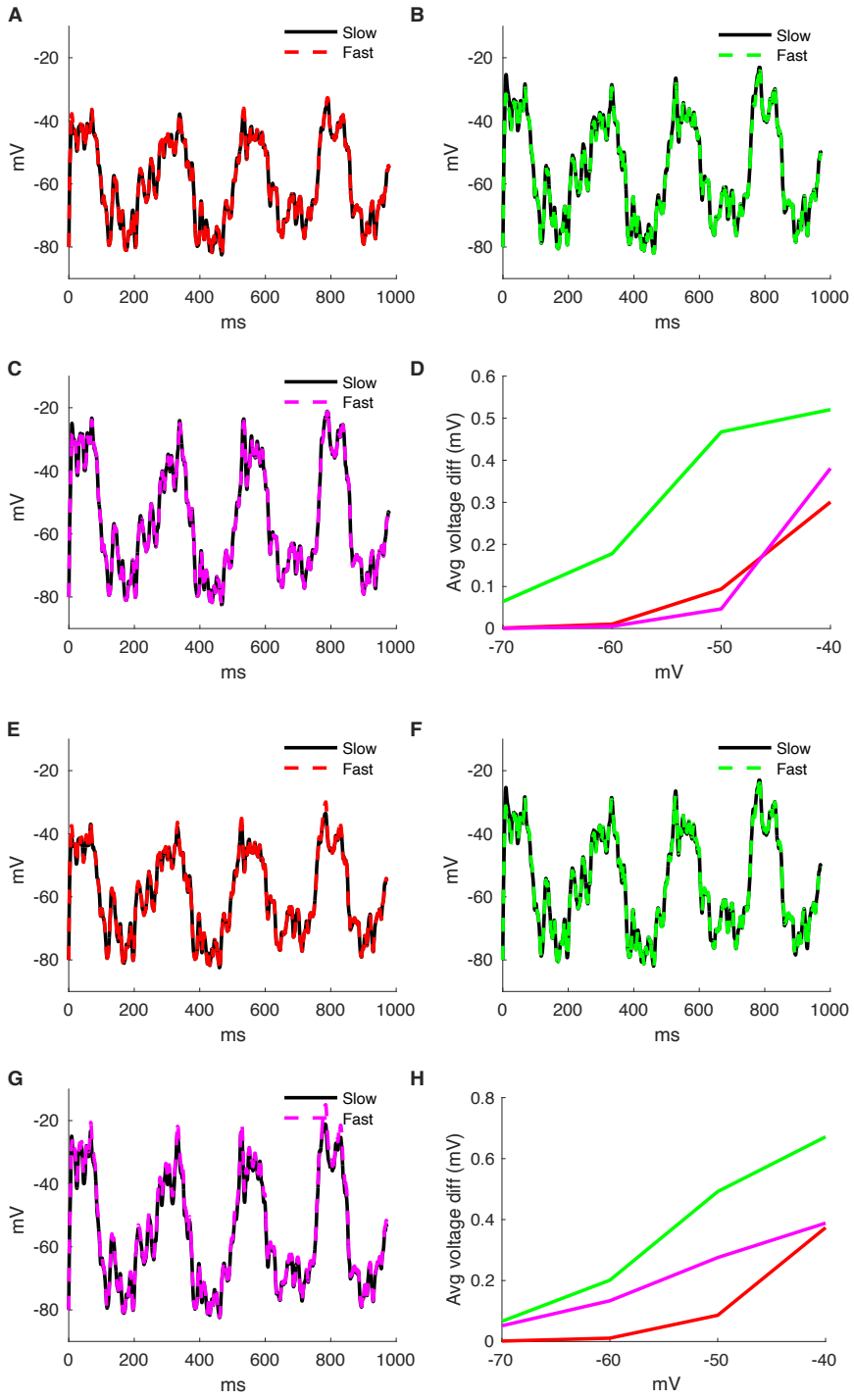

814

815 Fig 5. Comparison of traces using actual kinetics vs. fast kinetics (i.e. $\tau_{act} = \tau_{inact} = 0.1$ ms). A.

816 I_{KA}. B. I_{CaT}. C. I_{NaT}. D. Average voltage difference between the two tested conditions (I_{KA} in

817 red, I_{CaT} in green, I_{NaT} in magenta). Comparison of traces using actual activation/inactivation

818 variables and kinetics vs. fast kinetics (i.e. $\tau_{act} = \tau_{inact} = 0$ ms) and after linearizing inactivation

819 variables using activation variable for I_{KA} and I_{CaT} and power law approximation for I_{NaT}. E. I_{KA}.

820 F. I_{CaT}. G. I_{NaT}. H. Average voltage difference between the two tested conditions (I_{KA} in red, I_{CaT}

821 in green, I_{NaT} in magenta).

822

823

824

825

826

827

828

829

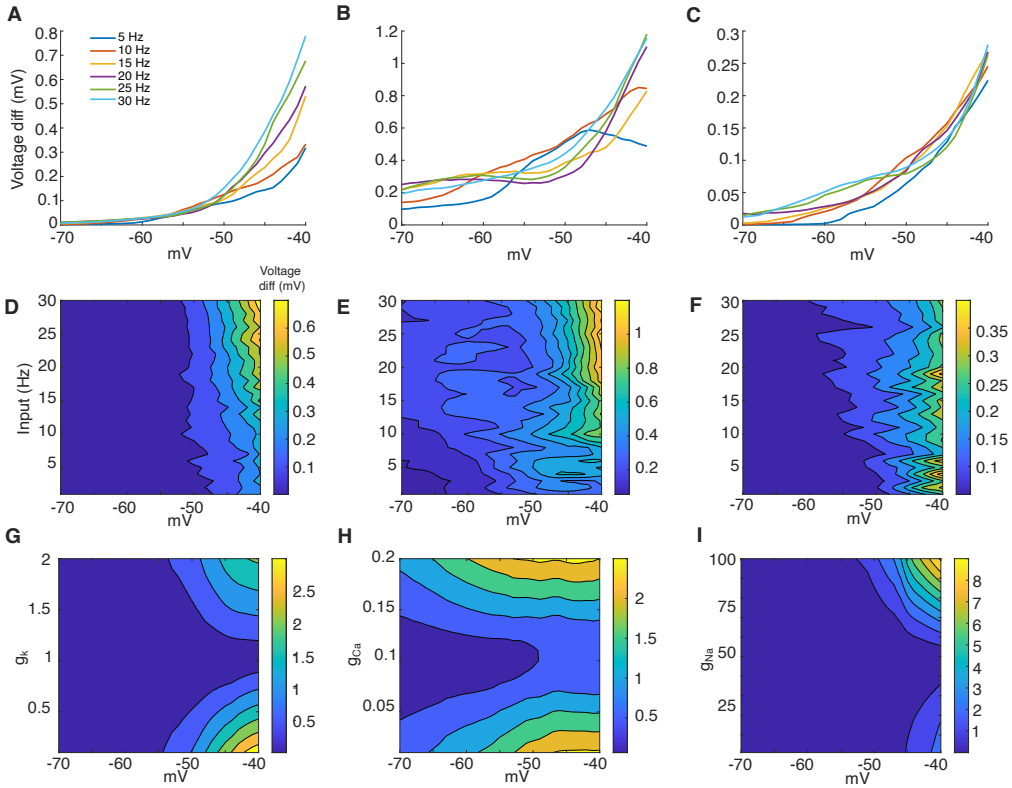

Fig 6. Voltage difference between the model with slow kinetics vs. instantaneous, when input frequency oscillations change from 1 to 30 Hz. A. I_{KA}. B. I_{CaT}. C. I_{NaT}. D. Heatmap of voltage difference between the model with slow kinetics vs instantaneous for voltages from -70 to -40 mV vs. input frequency oscillations change from 1 to 30 Hz for I_{KA}. E. I_{CaT}. F. I_{NaT}. G. Heatmap of the voltage difference between the model with slow kinetics vs instantaneous for voltages from -70 to -40 mV vs. I_{KA} conductance. E. I_{CaT} conductance. F. I_{NaT} conductance.

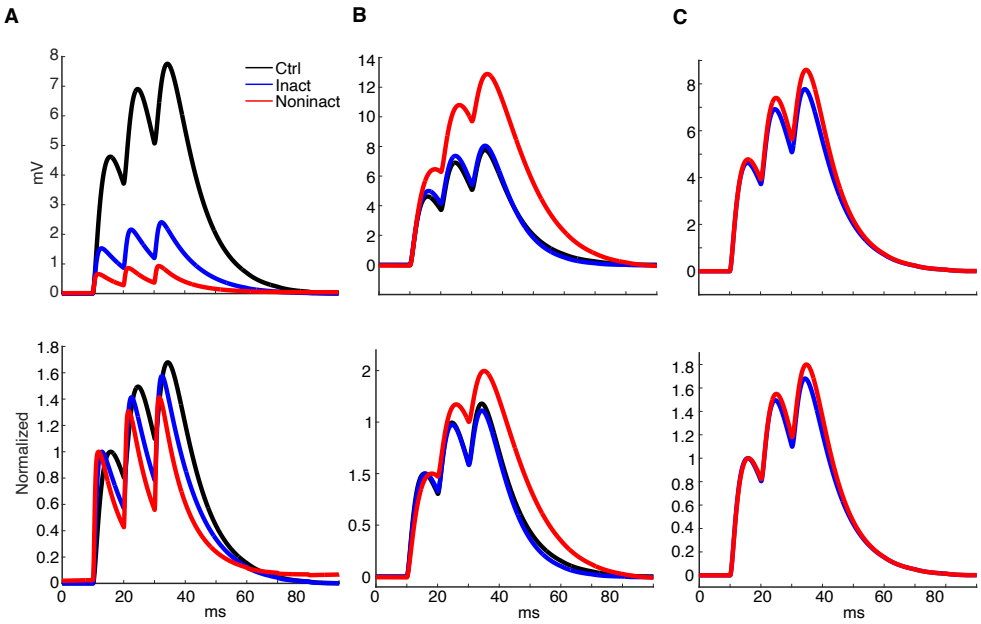

Fig 7. Inactivation and activation effects on summation. The voltage traces show summation for a train of 3 EPSPs. A. Model with I_{KA}. B. Model with I_{CaT}. C. Model with I_{NaT}. Initial resting membrane potential is -50 mV. Top: after baseline subtraction, bottom: after normalization. Three conditions were analyzed: only leak current (black), leak + inactivating current (blue), leak + noninactivating current (red).

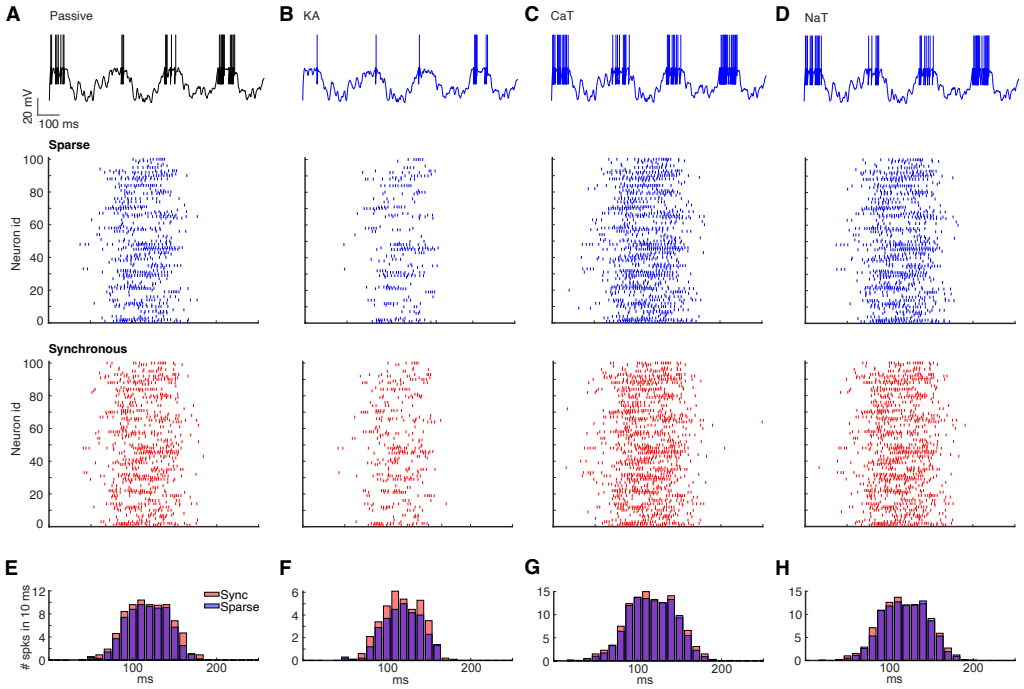

Fig 8. Synchrony- vs. rate-code and ionic currents dependency. Firing pattern under 4 Hz theta oscillations in a dendrite expressing A. only leak current. B. dendrite expressing only leak current plus I_{KA}. C. neuron expressing only leak current plus I_{CaT}. D. dendrite expressing only leak current plus I_{NaT}. (E, F, G, H) Raster plots and PSTH when stimulated with sparse input vs synchronous input.

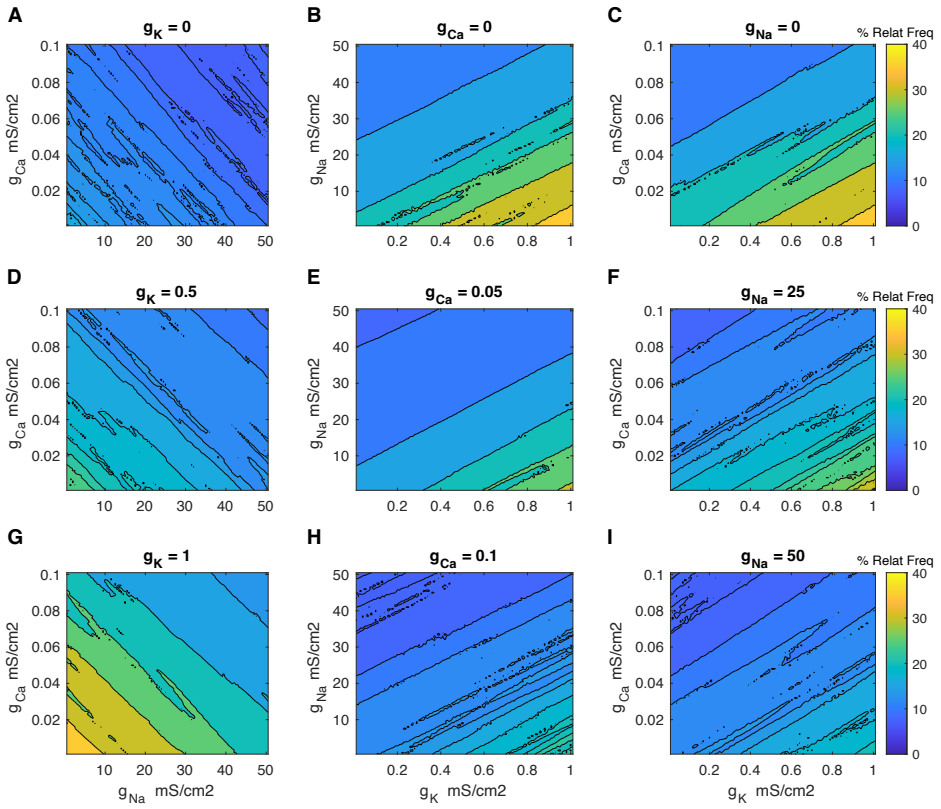

Fig 9. Heatmaps of % relat freq computed as difference between the sparse versus synchronized synaptic inputs spanned over different conductance values (see axis). A. I_{KA} vs I_{CaT} when gNa = 0. B. I_{KA} vs I_{NaT} when gCa = 0. C. I_{NaT} vs I_{CaT} when gK = 0. D. I_{KA} vs I_{CaT} when gNa = 25. E. I_{KA} vs I_{NaT} when gCa = 0.05. F. I_{NaT} vs I_{CaT} when gK = 0.5. G. I_{KA} vs I_{CaT} when gNa = 50. H. I_{KA} vs I_{NaT} when gCa = 0.1. I. I_{NaT} vs I_{CaT} when gK = 1. The % relat freq is an indicator of whether the dendrite acts as an integrator of coincidence detector (100% for perfect coincident detector and 0% for perfect integrator).

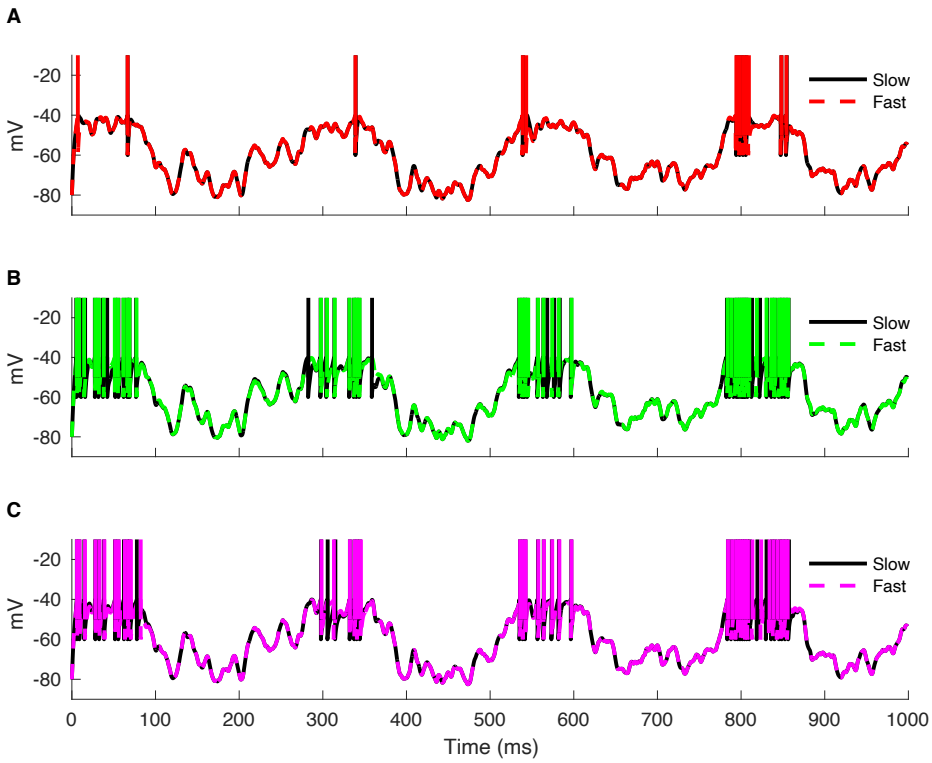

Suppl Fig 1. Comparison of spiking activity using actual kinetics vs fast kinetics (i.e. $\tau_{act} = \tau_{inact} =$ 0.1 ms). A. I_{KA}. B. I_{CaT}. C. I_{NaT}.

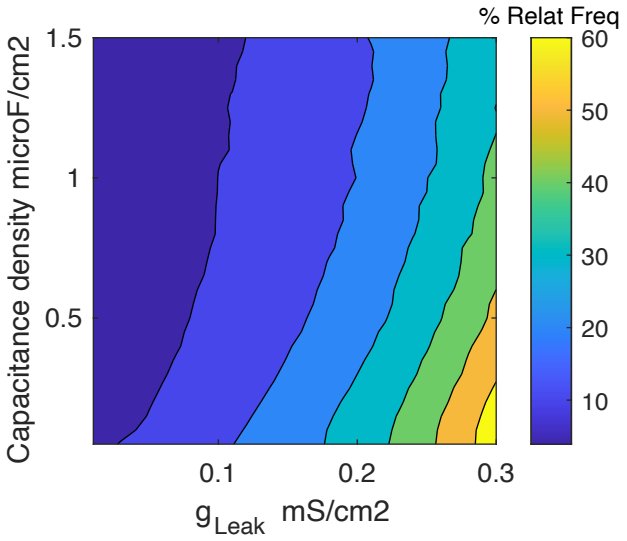

Suppl Fig 2. Heatmaps of % relat freq computed as difference between the sparse vs synchronized synaptic inputs spanned over different leak conductance values (x axis) vs capacitance density (y axis). The % relat freq is an indicator of whether the dendrite acts as an integrator of coincidence detector (100% for perfect coincident detector and 0% for perfect integrator).